Specialized medial prefrontal-amygdala coordination in prosocial and antisocial decision-making

Olga Dal Monte[1], Cheng-Chi J. Chu[1], Nicholas A. Fagan[1], Steve W. C. Chang[1,2,3,*]

1 Department of Psychology, Yale University, New Haven, CT 06520
2 Department of Neuroscience, Yale University School of Medicine, New Haven, CT 06510
3 Kavli Institute for Neuroscience, Yale University School of Medicine, New Haven, CT 06510
*Corresponding author: steve.chang@yale.edu

Abstract

Social behaviors recruit multiple cognitive processes requiring coordinated interactions among brain regions. Oscillatory coupling provides one mechanism for cortical and subcortical neurons to synchronize their activity. However, it remains unknown how neurons from different nodes in the social brain network interact when making social decisions. We investigated neuronal coupling between the rostral anterior cingulate gyrus (ACCg) of the medial prefrontal cortex and the basolateral amygdala (BLA) while monkeys expressed context-dependent prosocial or antisocial decisions impacting the reward of another monkey. We found an enhanced synchronization for prosocial decision preference between the two nodes, but a suppressed synchronization for antisocial decision preference. In support of a unique communication for prosocial decision-making, these interactions occurred in dedicated frequency channels depending on the area contributing spikes and had the opposite information flow directionalities for the two frequency channels. These findings support that specialized coordination in the medial prefrontal-amygdala network underlies social decision-making.

Introduction

Prosocial behaviors and mutually-beneficial social interactions facilitate social cohesion among members of a group and help attain collective rewards. While antisocial behaviors can be detrimental to these causes, they may be strategically necessary to secure limited resources or achieve a certain social status. The cognitive operations central to making such social decisions are theorized to recruit a wide array of brain regions that are sensitive to primary and more abstract rewards, and span both cortical and subcortical areas with divergent functional specifications[1–5].

Recent single-neuron studies using social interaction paradigms have begun to characterize neuronal correlates of social decision variables concerning conspecific animals in several brain regions. These regions include the anterior cingulate cortex (ACC)[6,7], the dorsomedial prefrontal cortex[8], the basolateral amygdala (BLA)[9–11], the orbitofrontal cortex (OFC)[6,12], the striatum[13], as well as the lateral prefrontal cortex[14,15]. Of these, the gyrus of the rostral ACC (ACCg) of the medial prefrontal cortex is thought to be particularly specialized in signaling rewarding and motivational information about social partners in both humans and monkeys[1,16]. Specifically, in a task where monkeys can display prosociality

by choosing to deliver juice rewards to a conspecific monkey over wasting the rewards, some ACCg cells exclusively encode conspecific's rewards while other cells encode one's own reward and conspecific's reward in an indistinguishable manner[6]. By contrast, neurons in the OFC or in the sulcus of the ACC in the same paradigm predominantly signal self-referenced decision variables by modulating firing rates only in relation to one's received or foregone rewards[6]. These findings lend a support for the role of rostral ACCg in computing other-referenced decision variables during social interactions[16]. On the other hand, BLA neurons, in the same behavioral task, exhibit systematically correlated firing rates for encoding monkey's choices that result in juice rewards allocated to either themselves or the conspecific monkey[9], suggesting that subcortical neurons in BLA utilize a shared metric for computing decision variables across self and other. These overall neural characteristics in relation to social decision variables have also later been observed in ACCg and BLA neurons in the human brain in an intracranial study[17]. While brain regions like ACCg and BLA are implicated in social decision-making, it is likely that the systematic communication across these and similar brain regions is what truly underlies such decisions.

Interactive communications across specific nodes in the social brain network likely plays a key role in social cognition. Whole-brain functional neuroimaging studies in humans have indicated the potential importance of correlated hemodynamic fluctuations across different brain regions in regulating complex social cognition[18,19]. In prairie voles, frequency-specific coupling between medial prefrontal cortex and nucleus accumbens is shown to mediate social bonding[20]. Moreover, ACC neurons in the medial prefrontal cortex network that directly project to BLA are found to be necessary for observational fear learning and social preference formation in mice[21]. In turn, dysregulated subcortical-medial prefrontal synchrony could result in abnormal social behaviors[22]. However, while there is growing evidence for the importance of interactive communication, neuronal mechanisms underlying interareal synchrony associated with complex social behaviors, such as those related to prosociality, remain elusive.

Reciprocally and densely innervating anatomical projections between ACCg and BLA permit the two nodes to efficiently communicate with one another for processing social and affective information[23,24]. However, whether and how ACCg and BLA coordinate their activity in relation to social decision-making remain unknown. If coordinated interactions between ACCg and BLA were involved in making either prosocial or antisocial decisions involving the welfare of others, one might expect distinctive coordination patterns exist for making prosocial compared to antisocial decisions. Such coordinated interaction may even occur through a dedicated frequency channel with a biased directionality of information flow between ACCg and BLA around the time of expressing social preferences. To directly test this hypothesis, we investigated how single-neuron spiking and local field potential (LFP) activity between ACCg and BLA are dynamically coordinated as monkeys expressed prosocial or antisocial decision preferences toward a conspecific monkey. We used spike-field coherence

as our primary measure as it quantifies how spikes from one brain region are synchronized with respect to specific temporal and oscillatory frequency of LFP activity from another brain region, allowing inspections of synchronous coordination of neural activity across brain areas[25,26].

We found that synchrony across spiking and LFP oscillations between the two nodes differentiated monkeys' prosocial decision preference in one context (enhanced spike-field coherence) from antisocial decision preference in another context (suppressed spike-field coherence). Moreover, specific frequency channels were recruited for the communications, with these frequency bands exhibiting selective directionality of information flow between the two nodes. Taken together, our findings demonstrate that unique rhythmic coordination of neuronal activity in the primate medial prefrontal-amygdala network contributes to context-specific social decision-making.

Results

Monkeys exhibit context-dependent prosocial and antisocial decision preferences

Pairs of rhesus macaques (an actor and a recipient) participated in the social reward allocation task (**Fig. 1a-b**; Online Methods). In one decision context (*Other*/*Bottle* context) where actor monkeys never received juice rewards, actors were free to choose between donating a juice drop to a recipient (*Other*) and to a juice collection bottle (*Bottle*). In the other decision context (*Self*/*Both* context) where actors always received juice rewards, actors were free to choose between delivering juice rewards to himself (*Self*) and to both himself and the other monkey (*Both*). There were three magnitudes of juice reward offered (Online Methods), and actors were informed of the value at stake on each trial. This task therefore measures actor's social decision preference without self-reward confound between the two available options in two separate contexts.

Actors completed 313 ± 109 (mean ± s.d.) trials per session across 57 sessions (monkey H: 374 ± 110 per session, 31 sessions; monkey K: 240 ± 43 per session, 26 sessions). Consistent with previous findings using this behavioral design[6,9,27,28], actors preferred to choose *Other* over *Bottle*, exhibiting a prosocial decision preference (preference index, mean ± s.e.m.: 0.32 ± 0.02, $p < 0.0001$, Wilcoxon sign rank) in the *Other*/*Bottle* context, but preferred to choose *Self* over *Both*, displaying an antisocial decision preference in the *Self*/*Both* context (–0.08 ± 0.02, $p < 0.001$) (**Fig. 1c**). These context-dependent preferences have been consistently observed across several different animals in independent studies[6,9,27,28], are sensitive to dominance and familiarity between pairs[27], and are abolished if the recipient monkey is replaced with a juice collection bottle[27].

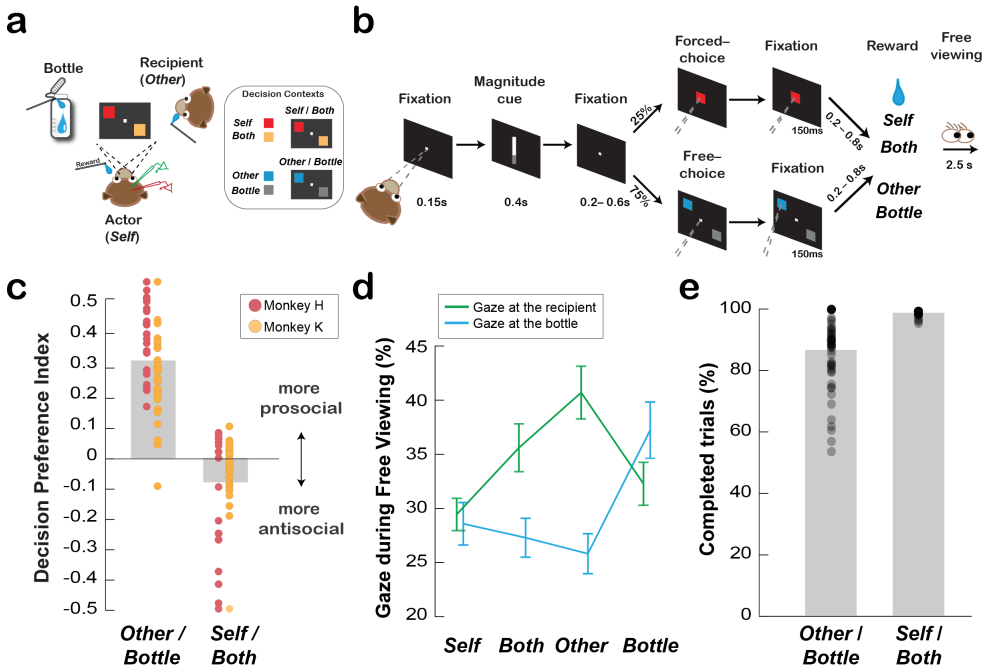

Fig. 1. Social reward allocation task and the behaviors associated with social decision preference. (**a**) Experimental setting involving an actor monkey, a recipient monkey, and an operating juice collection bottle. The inset shows example stimulus-reward outcome mappings for the two distinct contexts for rewarding the actor (*Self*) or both the actor and the recipient (*Both*) (*Self/Both* context), and for rewarding the recipient (*Other*) or the bottle (*Bottle*) (*Other/Bottle* context). (**b**) Task sequence for the social reward allocation task (Online Methods). (**c**) Monkeys exhibited context-dependent prosocial and antisocial preferences. Decision preferences are expressed as averaged contrast ratios for the two decision contexts. Data points overlaid on top show the biases for all individual sessions for each subject. (**d**) Social gaze patterns reflected decisions to deliver juice rewards to the recipient or the bottle as a function of different decisions. Shown are the mean (± s.e.m.) proportions of gaze to the recipient or to the bottle during the free viewing period for each reward outcome. (**e**) Average proportions of completed free-choice trials for *Other/Bottle* and *Self/Both* contexts. Data points show individual sessions.

Social gaze patterns differed as a function of decision (*Self*, *Both*, *Other*, *Bottle*) ($F[3, 455] = 2.86$, $p = 0.037$) and gaze-goal (the recipient or the bottle) ($F[1, 455] = 10.66$, $p = 0.001$). Critically, decision type and gaze-goal showed a strong interaction ($F[3, 455] = 8.75$, $p < 0.0001$), indicating that social gaze differed across decision types. Across all decision outcomes, actors looked at the recipient (36 ± 1% [mean ± s.e.m.]) at a higher rate than to the bottle (30 ± 1%, $p = 0.001$, Tukey test). Importantly, after choosing *Other,* actors looked at the recipient (41 ± 2%) more frequently compared to the bottle (26 ± 2%, $p < 0.0001$). By contrast, actors looked at the bottle more after choosing *Bottle* (37 ± 3%) than after choosing *Other* (26 ± 2%) ($p = 0.002$) (**Fig. 1d**). These observations support that actors were acutely aware of the reward outcome differences between the two conditions in which rewards were either allocated to the recipient or the bottle, the two outcomes without self-reward contingency[6,9,27,28].

As expected, actors overall completed more *Self/Both* trials (greater than 99% for all reward sizes) compared to *Other/Bottle* trials (87% for all reward sizes) ($F[1,341] = 175.12$, $p < 0.0001$) (**Fig.**

1e). However, actors were more motivated to complete *Other*/*Bottle* trials when the reward size at stake for either the recipient or the bottle was larger (small: 83 ± 2%, medium: 87 ± 2%, large: 90 ± 2%; $F[2,168] = 4.3$, $p = 0.02$). Moreover, actors were faster to choose targets associated with receiving rewards themselves (*Self* or *Both*) compared to forgoing rewards (*Other* or *Bottle*) ($p < 0.0001$, Wilcoxon rank sum). Taken together, the observed context-dependent social decision preferences of the actor monkeys provide a social behavioral framework for examining the coordination between ACCg and BLA neurons for prosocial and antisocial decision-making.

Coordination of spiking and LFP activity between ACCg and BLA

Exploiting monkey's context-dependent prosocial and antisocial preferences, we investigated neural coordination relating spiking and LFP activity for prosocial and antisocial decision preferences between rostral ACCg (Brodmann areas 24a, 24b, and 32)[29] and BLA (dorsal, intermediate, and ventrolateral basolateral complex)[29] (**Fig. 2**). All single units were recorded without any sampling criterion, resulting in 253 ACCg cells and 90 BLA cells. **Figure S1** shows the proportion of cells with significant modulations across time for all conditions in each region. As we have previously characterized single-cell encoding of social decision variables within ACCg and BLA in the identical social reward allocation task[6,9], here we focus on determining coordination in frequency and time between ACCg and BLA at the level of single cells and populations.

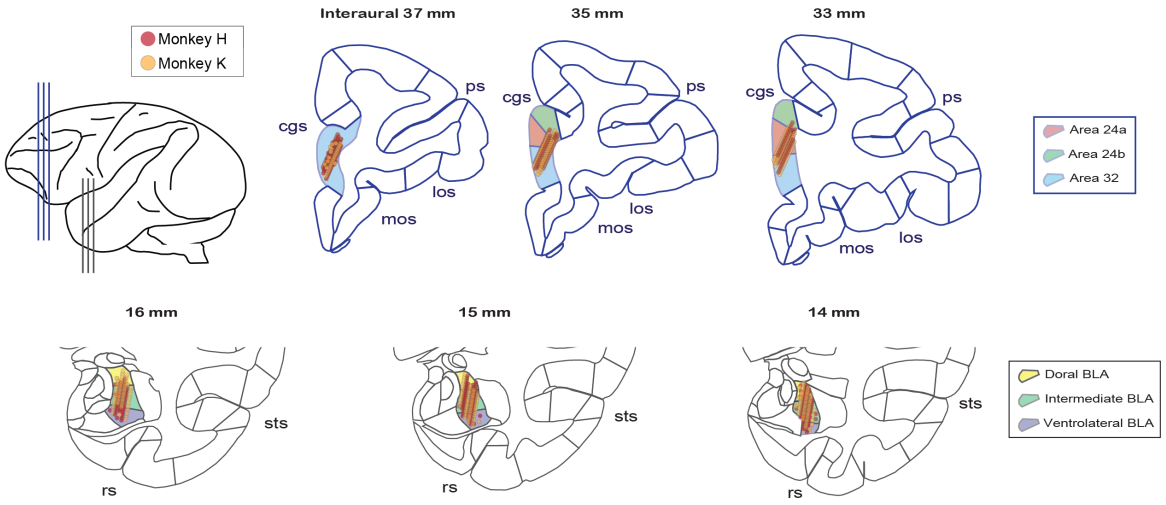

Fig. 2. Anatomical locations investigated for the coordination of spiking and LFP activity between BLA and ACCg. Recording locations for individual cells and LFP sites from monkey H (red points) and monkey K (orange points) projected onto the standard stereotaxic coordinates of the rhesus macaque brain atlas[29]. For each area's projections, three representative coronal slices were chosen with a 2-mm interaural spacing for ACCg and with a 1-mm interaural spacing for BLA in the anterior-to-posterior dimension (as shown in the top left cartoon). Selected landmarks are labeled: cingulate sulcus (cgs), principle sulcus (ps), medial orbitofrontal sulcus (mos), lateral orbitofrontal sulcus (los), superior temporal sulcus (sts), and rhinal sulcus (rs). Boxed insets show region assignments for the ACC Brodmann names and BLA subdivisions based on the Paxinos atlas[29].

To determine neuronal coordination between BLA and ACCg underlying social decision-making, we related spikes of individual cells from one area with LFP oscillations from the other area by calculating spike-field coherence from pairs of neurons and LFP sites[25,26]. Spike-field coherence values were computed from all recorded cells and LFP sites from which we collected the neural data without any selection criteria. This resulted in 253 ACCg cells paired with 268 BLA LFP sites and 90 BLA cells paired with 257 ACCg LFP sites. In this dataset, we investigated if the relations between spikes and fields, either $ACCg_{spike}$-BLA_{field} or BLA_{spike}-$ACCg_{field}$, systematically differed when monkeys expressed prosocial decision preference compared to antisocial decision preference. We analyzed coherence patterns during the 100 ms period centered on the time of acquiring a choice target on free-choice trials (decision epoch) and also during the 50–150 ms period after the central cue onset on forced-choice trials (cue epoch) for testing coherence patterns specific to active decision-making. Importantly, coherence values were always compared in a relative fashion (i.e., *Other* vs. *Bottle* for prosocial decision preference, and *Self* vs. *Both* for antisocial decision preference) such that any observed coherence differences were not confounded by actor's contingency for receiving a juice reward (i.e., actors never received rewards in the *Other*/*Bottle* context, but always received rewards in the *Self*/*Both* context).

Difference in spike-field coherence between prosocial decision preference (choosing *Other* over *Bottle*, *Other–Bottle*) and antisocial decision preference (choosing *Self* over *Both*, *Self–Both*) exhibited frequency-specific coordination as a function of the area that contributed spikes in the pair. Spikes from BLA cells and the LFP from ACCg (BLA_{spike}-$ACCg_{field}$) displayed enhanced coherence in the beta frequency range (defined here as 15–25 Hz) for prosocial decision preference ($p < 0.0001$, Wilcoxon sign rank) but suppressed coherence in the same band for antisocial decision preference ($p < 0.0001$) (difference between prosocial and antisocial decision preferences: $p < 0.0001$, Wilcoxon sign rank; **Fig. 3a-c** and **Fig. S2**). (**Figure 3a**, **3d**, and **3g** show the differences of spike-field coherence values between prosocial and antisocial decision preference, whereas **Figures 3b, 3e** and **S2** show spike-field coherence values for each decision preference separately.) This enhanced versus suppressed coherence difference was present immediately prior to the time of free-choice decision and lasted until around the time of completing the decision (i.e., fixating on the chosen target for a 150 ms duration after making the saccade to the target). By contrast, in the gamma frequency range (defined here as 45–70 Hz), spikes from ACCg cells and LFP from BLA ($ACCg_{spike}$-BLA_{field}) exhibited enhanced coherence, again, for prosocial decision preference ($p < 0.0001$) but suppressed coherence for antisocial decision preference ($p < 0.0001$) around the time of free-choice decision until around the time of completing the decision (difference: $p < 0.0001$; **Fig. 3d-f**). This coherence difference was present prior to the time of free-choice decision and lasted until around the time of completing the decision but this time course appeared to be lagged in time compared to the BLA_{spike}-$ACCg_{field}$ coherence in the beta band (**Fig. 3g**; described in more detail below). A resampling

procedure, in which, for each of 1000 iterations, 75% of randomly selected trials were used to recalculate spike-field coherence, produced consistent results, confirming that these results were not driven by outlier cells, sites, or trials (prosocial versus antisocial decision preference: BLA_{spike}-$ACCg_{field}$ coherence in the beta band, $p = 0.005$; $ACCg_{spike}$-BLA_{field} coherence in the gamma band, $p = 0.001$; Wilcoxon sign rank).

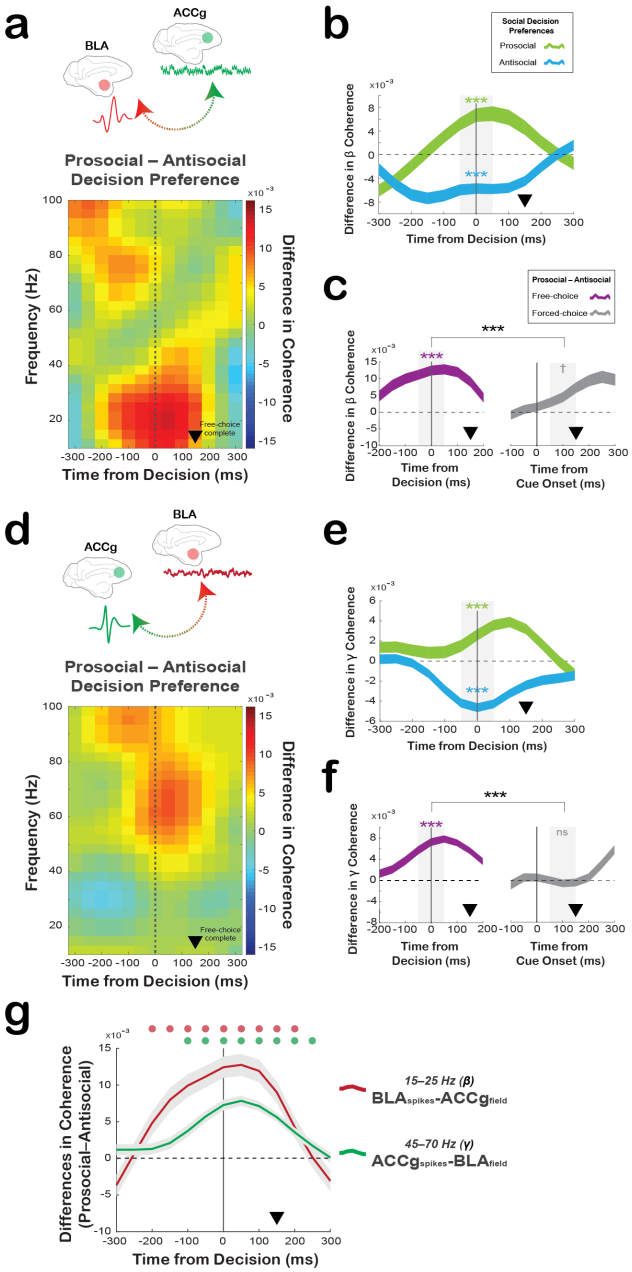

Fig. 3. Spike-field coherence between ACCg and BLA shows frequency-specific and free-choice-selective coordination for prosocial compared to antisocial decision preference. (**a**) Differences in BLA_{spike}-$ACCg_{field}$ coherence values between prosocial decision preference (*Other–Bottle*) and antisocial decision preference (*Self–Both*) across time and frequency aligned to the time of free-choice decision. (**b**) Time courses of the spike-field coherence values in the beta frequency separately for prosocial (light green; *Other–Bottle*) and antisocial (light blue: *Self–Both*) preferences. (**c**) Time courses of the beta spike-field coherence differences between prosocial and

antisocial decision preference on free-choice trials (purple) and between prosocial (*Other-forced–Bottle-forced*) and antisocial (*Self-forced–Both-forced*) forced-choice contrasts on forced-choice trials (grey). (**d**) Difference in $ACCg_{spike}$-BLA_{field} coherence values between prosocial and antisocial preference across time and frequency. Same format as in **a**. (**e**) Time courses of the spike-field coherence values in the gamma frequency separately for prosocial (light green) and antisocial (light blue) preferences. (**f**) Time courses of the gamma spike-field coherence differences between prosocial and antisocial decision preference on free-choice (purple) trials and between prosocial and antisocial forced-choice contrasts on forced-choice trials (grey). In **b**-**c** and **e**-**f**, significant coherence differences from zero (Wilcoxon sign rank) are indicated by asterisks in matching colors and significant coherence differences between traces (Wilcoxon rank sum) are indicated in black asterisks for the analyzed epoch (gray shading) (***, $p < 0.0001$; **, $p < 0.001$; †, $p = 0.07$; ns, not significant). (**g**) Average time courses of the beta band BLA_{spike}-$ACCg_{field}$ coherence (red) and the gamma band $ACCg_{spike}$-BLA_{field} coherence (green) differences between prosocial and antisocial decision preferences. Circles above the lines (in matching colors) show significant differences from zero ($p < 0.05$, Wilcoxon sign rank). In all plots, the black arrowheads mark the time at which the monkeys completed a free-choice or forced-choice decision by maintaining fixation on a chosen target or cue for 150 ms.

Moreover, to establish if these observed coherence patterns were specific for relating spikes and LFPs rather than were simply driven by a more global-level synchrony or by a common input signals, we examined field-field coherence between the two areas. We obtained qualitatively different coherence patterns with respect to both the timing and the direction of coherence modulation (enhancement versus suppression) between LFPs across the two areas (**Fig. S3** and Supplemental Results). Further, within-region spike-field coherence patterns also showed qualitatively different patterns from the observed between-region spike-field coherence (**Fig. S4** and Supplemental Results). Taken together, these findings supporting unique communication patterns involving spikes and fields between the two areas.

Crucially, the coordination of spikes and LFP observed between BLA and ACCg was specific to when the actor monkeys made preference-based decisions (free-choice). From pseudo-randomly interleaved forced-choice trials in which the computer selected the reward outcomes that were otherwise identical, we were able to construct spike-field coherence differences with matching reward outcomes in the absence of decision-making. We contrasted *Other-forced* and *Bottle-forced* trials (prosocial forced-choice contrast) for comparing it to prosocial decision preference and contrasted *Self-forced* and *Both-forced* trials (antisocial forced-choice contrast) for comparing it to antisocial decision preference. The beta band BLA_{spike}-$ACCg_{field}$ coherence as well as the gamma band $ACCg_{spike}$-BLA_{field} coherence markedly differed between when the monkeys did or did not make active decisions (**Fig. 3c**, **f**, and **Fig. S2**). The beta BLA_{spike}-$ACCg_{field}$ coherence (15–25 Hz), which was selectively enhanced for prosocial decision preference ($p < 0.0001$, Wilcoxon sign rank), was much weaker for prosocial forced-choice contrast ($p = 0.07$) (difference between free-choice and forced-choice: $p < 0.0001$, Wilcoxon rank sum). Similarly, the gamma $ACCg_{spike}$-BLA_{field} coherence (45–70 Hz), which was again selectively enhanced for prosocial decision preference ($p < 0.0001$), was absent for prosocial forced-choice contrast ($p = 0.15$) (difference between free-choice and forced-choice: $p < 0.0001$). Therefore, the coordination signatures differentiating

247 prosocial from antisocial decision preference were unique to making free-choice decisions and not merely
248 driven by either the visual stimuli or the anticipation of specific reward outcomes.
249 Given that the BLA_{spike}-$ACCg_{field}$ coherence differences in the beta band appeared to emerge
250 earlier and terminated sooner than $ACCg_{spike}$-BLA_{field} coherence differences in the gamma band (**Fig. 3**),
251 we next examined possible disparities in the coherence onset time to help elucidate any potential
252 functional differences between the two coordination types. The BLA_{spike}-$ACCg_{field}$ coherence in the beta
253 band began to significantly differentiate prosocial from antisocial decision preference earlier ($p < 0.05$,
254 Wilcoxon sign rank) than the $ACCg_{spike}$-BLA_{field} coherence in the gamma band (**Fig. 3g**). Additionally, the
255 $ACCg_{spike}$-BLA_{field} coherence in the gamma band continued to significantly differentiate prosocial from
256 antisocial decision preference longer compared to BLA_{spike}-$ACCg_{field}$ coherence in the beta band (**Fig. 3g**).
257 The BLA_{spike}-$ACCg_{field}$ communication in the beta band may thus represent an earlier stage of the
258 interactive communication between the two areas in favor of prosocial over antisocial decision
259 preference. Finally, we tested if there were any anatomical differences in the strength of spike-field
260 coherence patterns. We found no discernable anatomical gradients for either the beta or gamma spike-
261 field coherence differences between prosocial and antisocial decision preferences within ACCg and BLA
262 cells/sites (all comparisons using AP, ML, or Depth dimension separately, or based on principal
263 component analysis, all $|r| < 0.32$, all $p < 0.16$, Spearman correlation).
264
265 **Directionality of information flow between ACCg and BLA for social decisions**
266 Communications between ACCg and BLA may exhibit a specific directionality of information
267 flow that may critically differ between making prosocial and antisocial decisions. To determine this, we
268 performed a partial directed coherence (PDC) analysis, a specialized methodology derived from the
269 Granger analytic principle purposely tailored for analyzing directionality in the frequency-time domain[30].
270 Without choosing any frequency bands a priori, we observed systematic differences in directional
271 information flow between ACCg and BLA as a function of social decision preference as well as
272 frequency band. We found a significant influence of BLA to ACCg in the beta band (BLA→ACCg) for
273 prosocial decision preference, the same frequency range that exhibited an increase in the BLA_{spike}-
274 $ACCg_{field}$ coherence for prosocial decision preference (PDC difference between BLA→ACCg and
275 ACCg→BLA, $p = 0.03$; Wilcoxon sign rank) (**Fig. 4a, b**). However, we did not observe any systematic
276 directionality associated with antisocial decision preference (PDC difference, $p = 0.74$) (**Fig. 4a, b**). By
277 contrast, information flow in the gamma band, which showed an increase in the $ACCg_{spike}$-BLA_{field}
278 coherence for prosocial decision preference, instead occurred from ACCg to BLA (ACCg→BLA) for
279 prosocial decision preference (PDC difference between ACCg→BLA and BLA→ACCg, $p < 0.01$), but
280 again with no systematic directionality for antisocial decision preference (PDC difference, $p = 0.57$) (**Fig.**

4a, b). In fact, for antisocial decision preference, we did not observe any PDC directionality between BLA and ACCg in all tested frequency bands (all comparisons, $p > 0.05$; **Fig. 4b**). Notably, the BLA→ACCg directionality in the beta band and the ACCg→BLA directionality in the gamma band matched remarkably well with the frequency ranges found in the spike-field coherence selective to prosocial decisions. Finally, we observed pronounced differences in both BLA→ACCg and ACCg→BLA PDC values for free-choice compared to forced-choice trials for prosocial decision preference, but generally not for antisocial decision preference (**Fig. 4c** and **Fig. S5**). Together, these findings demonstrate the presence of specific information flow directions between ACCg and BLA for expressing prosocial decision preference. Even though the PDC analyses do not use spikes, the beta band was associated with the information flow from BLA to ACCg and the enhanced BLA_{spike}-$ACCg_{field}$ coherence, whereas the gamma band was associated with the information flow from ACCg to BLA and the enhanced $ACCg_{spike}$-BLA_{field} coherence, with both measures in each case being prioritizing prosocial decision preference.

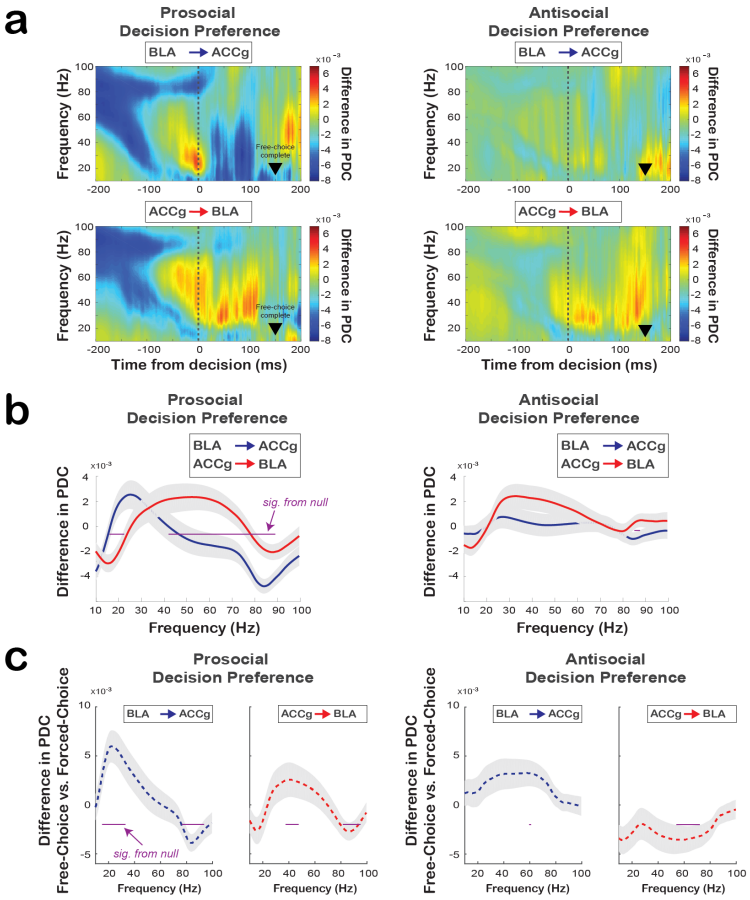

Fig. 4. Directionality of information flow between ACCg and BLA for prosocial and antisocial decision preferences as a function of time and frequency. (**a**) Frequency-domain directional influences assessed by partial directed coherence (PDC) on free-choice trials. PDC values as a function of time and frequency for prosocial decision preference (*Other–Bottle*) for BLA→ACCg (top left) and ACCg→BLA (bottom left), and PDC values for

antisocial preference (*Self–Both*) for BLA→ACCg (top right) and ACCg→BLA (bottom right). The black arrowheads mark the time at which the monkeys completed a free-choice by maintaining fixation on a chosen target for 150 ms. (**b**) Quantification of the directionality of information flow during the free-choice decision epoch as a function of frequency for prosocial decision (left) and antisocial decision preferences (right) for BLA→ACCg (in blue) and ACCg→BLA (in red). Horizontal purple lines indicate significantly different PDC values from the empirically derived null distribution ($p < 0.05$, Wilcoxon sign rank). Shaded regions represent s.e.m. (**c**) Differences in PDC values between free-choice trials (active decision-making) and forced-choice trials (computer-determined outcomes) for prosocial decision (two plots on the left) and antisocial decision preference (two plots on the right). Same format as in **b**.

Decoding social decisions directly from synchrony between ACCg and BLA

To examine whether neuronal coordination between ACCg and BLA contain decodable information on monkey's social decisions, we trained a linear decoder to discriminate decision types directly from observed spike-field coherence values (**Fig. 3**). The classifier was trained using randomly selected 75% of trials and later tested on the remaining 25% of trials used as inputs, yielding estimates of the decision outcome on each trial.

The first decoder was trained to distinguish between *Other* and *Bottle* decisions (prosocial decision preference) from the BLA_{spike}-$ACCg_{field}$ coherence values in the beta band (15–25 Hz) or from the $ACCg_{spike}$-BLA_{field} coherence values in the gamma band (45–70 Hz) across time. Decoding performance from the beta BLA_{spike}-$ACCg_{field}$ coherence for discriminating *Other* from *Bottle* began to increase prior to the decision time and peaked around the time of the decision ($p < 0.0001$, compared to an empirically-derived null distribution, Wilcoxon sign rank) (**Fig. 5a**). On the other hand, the decoding accuracy from the gamma $ACCg_{spike}$-BLA_{field} coherence for discriminating *Other* from *Bottle* was lower at the time of free-choice decision but gradually improved as monkeys fixated on a chosen option during the time required to complete the decision (**Fig. 5b**). The second decoder was trained to now distinguish between *Self* and *Both* for classifying antisocial decision in the identical frequency bands and times. In sharp contrast to the first decoder, the decoding performance was overall lower around the time of free-choice decision, albeit still being able to decode above its empirically-derived chance level (**Fig. 5a**, **b**). Directly comparing decoder accuracy between the two decision contexts revealed that *Other*/*Bottle* discriminability was higher than *Self*/*Both* discriminability when decoding from the beta BLA_{spike}-$ACCg_{field}$ coherence compared to the gamma $ACCg_{spike}$-BLA_{field} coherence at the time of decision (100 ms centered on the decision time, $p < 0.0001$, Wilcoxon rank sum) (**Fig. 5c**). However, as the monkeys continued to fixate on a chosen target to complete the decision (from 50 to 150 ms), this pattern reversed such that the gamma $ACCg_{spike}$-BLA_{field} coherence now exhibited higher *Other*/*Bottle* discriminability compared to the beta BLA_{spike}-$ACCg_{field}$ coherence ($p < 0.0001$) (**Fig. 5c**). These temporal differences in decoding accuracy are consistent with the temporal differences observed between the beta BLA_{spike}-$ACCg_{field}$ and the gamma $ACCg_{spike}$-BLA_{field} coherence differences in favor of prosocial decision

preference. Overall, although the extent of decoding accuracy for predicting monkey's social decisions was low even at the peak accuracy level (< 60%), decoding directly from the synchrony signatures was nevertheless reliable.

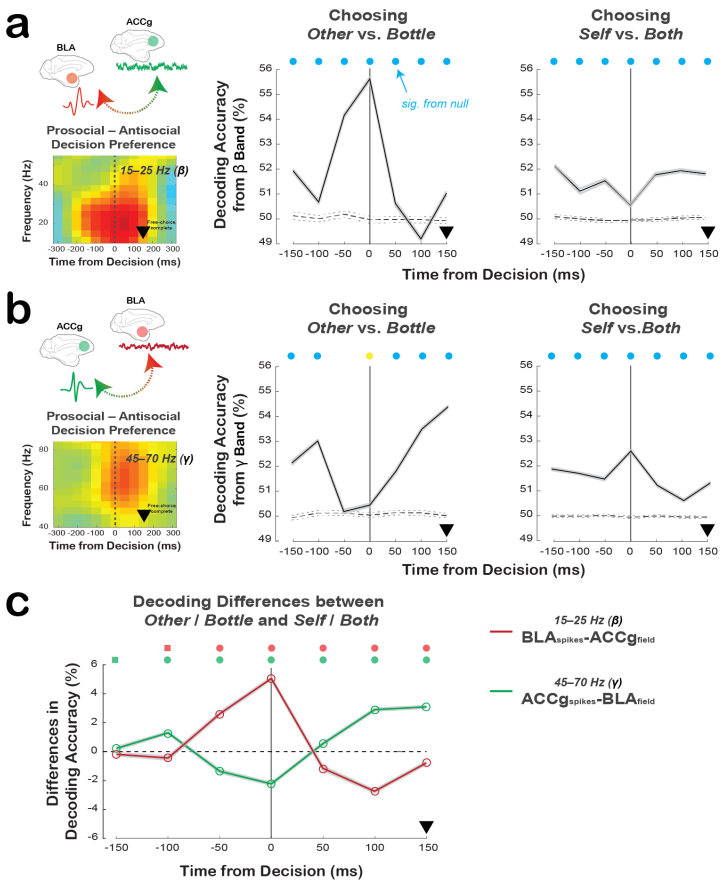

Fig. 5. Decoding social decisions directly from the spike-field relations between ACCg and BLA. (**a**) Decoding performance using the BLA_{spike}-$ACCg_{field}$ coherence differences in the beta band (shown in the left inset) for discriminating *Other* from *Bottle* (middle) and discriminating *Self* from *Both* (right) decisions over time (mean ± s.e.m.). Dashed lines represent empirically determined null distribution. Circles above the lines indicate significant differences from the null in each of the 50 ms bin (blue: $p < 0.001$, yellow: $p < 0.05$, Wilcoxon sign rank). (**b**) Average decoding performance using the $ACCg_{spike}$-BLA_{field} coherence in the gamma band (shown in the left inset) for discriminating *Other* from *Bottle* (middle) and discriminating *Self* from *Both* (right) decisions over time. Same format as in **a**. (**c**) Differences in decoding performances between *Other*/*Bottle* and *Self*/*Both* contexts from the beta BLA_{spike}-$ACCg_{field}$ coherence (red) and the gamma $ACCg_{spike}$-BLA_{field} coherence (green). Symbols above the lines (in matching colors) show significant differences from zero (circles: $p < 0.0001$, square, $p < 0.05$; Wilcoxon sign rank). In all plots, the black arrowheads mark the time at which the monkeys completed a free-choice decision by maintaining fixation on a chosen target for 150 ms.

Discussion

Coordination through oscillatory mechanisms has been theorized to provide a unique temporal window for neuron-to-neuron communications[31–33]. Growing evidence supports that oscillatory coordination across different brain regions is one mechanism used to regulate a wide range of cognitive

360 functions, ranging from visual perception[34,35], motor planning[36], and spatial navigation[37] to higher-order
361 functions underlying working memory[38], associative learning and decision-making[39–42]. A number of
362 studies have also emphasized the importance of cortical-subcortical interactions in facilitating complex
363 cognitive operations[20,21,24,40–42]. Frequency-specific and direction-selective coordination between ACCg
364 and BLA cells reported here exemplifies one possible medial prefrontal-amygdala coordination
365 mechanism by which two nodes in the social brain network interact during complex social behaviors.

366 The coherence patterns between ACCg and BLA were predominantly characterized by enhanced
367 coherence for prosocial decision preference but suppressed coherence for antisocial decision preference
368 (**Fig. 3**). Thus, enhanced engagements between ACCg and BLA may promote the expression of prosocial
369 preference, whereas disengagements between ACCg and BLA in turn may lead to the expression of
370 antisocial preference. Notably, the coordination patterns exhibited specializations in the frequency
371 domain. The beta band was involved in linking spiking outputs from BLA cells with the synaptic input or
372 dendritic integration of ACCg cells, whereas the gamma band was involved in the interaction linking
373 these processes in reverse. Frequency-specific coordination between ACCg and BLA may provide
374 separate communication streams that should be useful for differentiating social decision preferences. Such
375 specializations of frequency channels underlying different cognitive operations have also been observed
376 in the past for cortico-cortical interactions involving top-down and bottom-up visual attention[43].

377 In general, synchrony found in lower frequency range is thought to be more robust to temporal
378 dynamics of spiking activity due to slower temporal profiles[44], perhaps making lower frequency channels
379 better for synchronizing distant structures. Further, the beta frequency in particular has been theorized to
380 mediate 'the status quo' functions associated with maintaining predicted or internally-consistent
381 behaviors[45]. The use of beta frequency channel for linking BLA spikes to ACCg fields may indicate one
382 mechanism for facilitating robust and long-range communications between BLA and ACCg for the
383 consistently preferred prosocial decision preference. On the other hand, synchrony found in higher
384 frequency range is likely be strongly driven by local computations, requiring fast-spiking GABA-ergic
385 inhibitory interneurons[44,46]. The gamma frequency especially has been associated with generating
386 selective representations of certain stimuli over others[47]. The use of gamma frequency channel for linking
387 ACCg spikes to BLA fields is likely to be driven by local computations necessary following the long-
388 range communications initiated through the beta frequency.

389 Importantly, the directionality of information flow between the two regions was largely selective
390 for prosocial decision preference, with difference information flow directions between the beta and
391 gamma frequency bands. These information flow directions corresponded very well to an inferred
392 directionality based on the spike-field coherence within the same frequency range, if we presume that the
393 spikes from one area send information to the other area in a given pair of reciprocally-connected areas.

394 Selectively for prosocial decision preference over antisocial decision preference, the beta band facilitated
395 the information flow from BLA→ACCg and exhibited enhanced BLA_{spike}-$ACCg_{field}$ coherence, whereas
396 the gamma band facilitated the ACCg→BLA information flow and showed enhanced $ACCg_{spike}$-BLA_{field}
397 coherence. These findings converge to support that BLA cells communicate with ACCg using the beta
398 channel while ACCg cells communicate with BLA using the gamma channel, and that these interactions
399 are selective for expressing prosocial decision preference.

400 Prior single-unit studies have found that value tuning functions in BLA cells are highly correlated
401 between self and other when monkeys make social decisions[9], whereas ACCg cells signal decision
402 variables largely in an agency-specific manner (self-referenced or other-referenced reward outcome
403 coding)[6]. Similar neuronal properties are found in the human amygdala and ACCg in social contexts[1,16].
404 Overall, medial prefrontal regions compute agent-specific decision variables, whereas subcortical regions
405 compute decision variables in an agent-integrated manner[6,8,9]. Generalized coding of social value in BLA
406 and an agent-specific coding of reward outcome in ACCg suggest that value for prosocial decision may
407 be initiated by BLA prior to being transformed into an agency-specific reward outcome representation in
408 ACCg and other medial prefrontal cortical areas. Indeed, the BLA-ACCg coordination that differentiated
409 prosocial from antisocial decision preference first emerged between BLA spikes and ACCg fields in the
410 beta band compared to the coordination in the reverse direction (**Fig. 3**). Further, decisions for donating
411 juice rewards to the recipient or the bottle was predicted earlier from the beta BLA_{spike}-$ACCg_{field}$
412 coherence compared to the gamma $ACCg_{spike}$-BLA_{field} coherence (**Fig. 5**). BLA cells are known for
413 signaling social contextual information, such as distinct social gaze orientations and facial
414 expressions[48,49], that powerfully shapes social interactions. Future work can test if and when BLA cells
415 transmit such information to rostral ACCg or other medial prefrontal cortical areas to bias social decisions
416 across various social contexts.

417 Finally, the coordination between ACCg and BLA were largely selective to free-choice or active
418 decisions, compared to when the computer made the decisions for the actors. This finding strongly argues
419 that the coordination between these areas were not driven by upcoming reward outcomes, but rather
420 driven by voluntarily expressing one's social decision preferences. Freely expressing social preference
421 may therefore engage the medial prefrontal-amygdala circuit in unique ways. This hypothesis is also
422 supported by two previous observations in the primate BLA demonstrating specialized neural codes for
423 computing free-choice, compared to forced-choice, decisions[9,50].

424 Overall, the current findings support the view that ACCg and BLA neurons utilize distinct
425 frequency channels and direction-selective communications for social decision-making. Efficient and
426 perhaps even strategic coordination occurring between medial prefrontal regions and the amygdala that
427 prioritizes prosocial over antisocial preference may play an essential role in promoting mutually

beneficial social cohesion. In turn, failures in synchronized transmissions along the medial prefrontal-amygdala network may bias other relevant brain networks to converge toward producing atypical social interactions.

Data Availability

Behavioral and neural data presented in this paper and the main analysis codes will be available through https://github.com/changlabneuro.

Acknowledgements

We are extremely grateful to Bijan Pesaran for his guidance on examining oscillatory neural processes throughout the duration of this research. We especially thank Daeyeol Lee and Alex Kwan for their thoughtful discussions and suggestions on improving this work. We also thank Amrita Nair and Siqi Fan for insightful comments on the manuscript. This work was supported by the National Institute of Mental Health (R01MH110750; R21MH107853; R00MH099093), Alfred P. Sloan Foundation (FG-2015-66028), and the Teresa Seessel Postdoctoral Fellowship.

Author Contributions

S.W.C.C. and O.D.M. designed the study and wrote the paper. O.D.M. performed the experiments. C.J.C., N.A.F., O.D.M., and S.W.C.C. analyzed the data.

Competing Financial Interests

The authors declare no competing financial interests.

451 # Methods

452

453 **Animals**

454 Two adult male rhesus macaques (*Macaca mulatta*) were involved in the study as actors
455 (monkeys K and H; ages, both 6; weights, 7 and 8 kg), and two adult female monkeys (ages, 6 and 10;
456 weights, 9 and 10 kg) were involved only as recipients in the social reward allocation task. All animals
457 were unrelated and not cagemates. Actors were housed in a colony room with other male macaques,
458 whereas two female macaques resided in an adjacent colony room with other females. All four subjects
459 were housed in pairs with other animals from the colony, kept on a 12-hr light/dark cycle, had
460 unrestricted access to food, and controlled access to fluid during testing. All procedures were approved by
461 the Yale Institutional Animal Care and Use Committee and in compliance with the National Institutes of
462 Health Guide for the Care and Use of Laboratory Animals.

463

464 **Surgery and anatomical localization**

465 All four animals received a surgically implanted headpost (Grey Matter Research) for restraining
466 their head during the experiments. Subsequently, a second surgery was performed on actor monkeys to
467 implant a recording chamber (Crist) to provide access to ACCg and BLA. Placement of the chambers
468 were guided by both structural magnetic resonance imaging (MRI) scan and stereotaxical coordinates.
469 Prior to starting the recording experiments, we performed a manganese (Mn)-enhanced magnetic
470 resonance imaging (MEMRI) session for each actor monkey to precisely localize our recording sites in
471 both ACCg and BLA. For MEMRI, we focally infused 2 μl of 19.8 μg/μl of Mn (manganese (II) chloride)
472 in saline solution in both areas using modified Hamilton syringes that traveled along the identical
473 trajectory as our electrodes. We then performed a structural MRI scan 3 hours after the infusion to
474 visualize a bright halo to confirm anatomical locations[51]. All electrophysiological recordings were carried
475 out simultaneously from ACCg (Brodmann areas 24a, 24b, and 32)[29] and BLA (dorsal, intermediate, and
476 ventrolateral basolateral complex)[29] (**Fig. 2**).

477

478 **Social reward allocation task**

479 Two monkeys (an actor and a recipient) sat in primate chairs (Precision Engineering, Inc.) at 100
480 cm from one another at a 90° angle (**Fig. 1a**). Each monkey had his own monitor, which displayed
481 identical visual stimuli. Both monkeys had their own juice tubes from which juice drops were delivered
482 via solenoid valves. A third juice tube with its own dedicated solenoid valve delivered juice rewards into
483 an empty bottle (*Bottle*), which was placed on the opposite side of the recipient (**Fig. 1a**). To prevent
484 monkeys from forming secondary associations of solenoid clicks, the three solenoid valves were placed in

another room and white noise was played in the background during all experimental sessions. An infrared eye-tracking camera (EyeLink 1000, SR Research) continuously recorded the horizontal and vertical eye positions from actor monkeys.

An actor began a trial by fixating on a central square for 150 ms with gaze. The reward value at stake on each trial was specified by a magnitude cue displayed as a vertical bar indicating juice volume (0.2, 0.4, or 0.6 ml). The actor was required to maintain gaze fixation on the magnitude cue for 400 ms. Following a variable delay (200, 400, or 600 ms), the actor was presented with either a free-choice (75%) or a forced-choice (25%) trial. On free-choice trials, two visual targets appeared at two random peripheral locations on opposite sides of the screen. The actor had 2 sec to make a choice by shifting gaze to a target and maintaining the fixation on the target for additional 150 ms in order to complete a choice (i.e., any break in gaze fixation resulted in an incomplete trial with no further progression into the trial). These choice targets were always presented in two distinct contexts presented pseudo-randomly. In the *Self*/*Both* context (50% of free-choice trials), the actor made decisions to deliver a juice drop to himself (*Self*) or both himself and the recipient monkey (*Both*; the same amount was delivered at the same time to both monkeys). By contrast, in the *Other*/*Bottle* context (50% of free-choice trials), the actor made decisions to deliver a juice drop to the recipient monkey (*Other*) or to the empty juice collection bottle (*Bottle*). Critically, any choice made in the two contexts were 'reward-matched' from actor's perspective such that the actor always received a reward in the *Self*/*Both* context but never received a reward in the *Other*/*Bottle* context. After a following variable delay from completing the decision (200, 400, 600, or 800 ms), a juice reward corresponding to the chosen target was delivered to himself (*Self*), to the recipient (*Other*), to both monkeys (*Both*), or to the bottle (*Bottle*). On forced-choice trials, only a single central cue was presented on the screen, and the actor had to simply maintain the fixation for 150 ms to complete the forced-choice decision (i.e., any break in fixation resulted in an incomplete trial with no further progression into the trial). These computer-determined reward outcomes occurred with equal frequency, pseudorandomly ordered. After a following variable delay (200, 400, 600, or 800 ms), a juice reward corresponding to the central cue was delivered to himself (*Self-forced*), to the recipient (*Other-forced*), to both monkeys (*Both-forced*), or to the bottle (*Bottle-forced*). For both free-choice and forced-choice trials, reward delivery was followed by a 2.5 sec inter-trial interval, during which the actor was free to look at the recipient or any other locations in the setup. A trial was considered incomplete if the actor failed to choose a target or maintain the required 150 ms fixation on free-choice trials or to maintain the required 150 ms fixation on the cue on forced-choice trials. The incomplete trials were not included in the analyses.

Electrophysiology

LFP and spiking activity was recorded using 16-channel axial array electrodes (U- or V-Probes, Plexon) or single tungsten electrodes (FHC Instruments) placed in each of the recording regions using a 32-channel system (Plexon). At the beginning of each session, a guide tube was used to penetrate the intact dura and to guide electrodes, which were lowered using a motorized multi-electrode microdrive system (NaN Instruments) with a speed of 0.02 mm/sec. After the electrodes reached the target sites in both ACCg and BLA, we waited 30 min for the tissue to settle before starting each recording session to ensure signal stability. Because some of the data were obtained using two 16-channel electrode arrays, one in ACCg and the other in BLA (20% of the total recording sessions), we randomly assigned 16 uniquely paired LFP sites across the two regions, using a random number generator, to remove redundant inflations of correlation for the relevant data.

Data Analysis

Behavioral analyses

To quantify prosocial and antisocial decision preferences, we constructed a choice preference index as contrast ratios[6,27,28,52] (Eq. 1).

$$Preference\ Index = \frac{R_a - R_b}{R_a + R_b} \quad \text{(Eq. 1)}$$

R_a and R_b were the frequency of particular choices. For the *Self*/*Both* context, R_a and R_b were numbers of *Self* and *Both* choices, respectively. For the *Other*/*Bottle* context, R_a and R_b were numbers of *Other* and *Bottle* choices, respectively. An index of 1 thus corresponds to always choosing a prosocial outcome, –1 corresponds to always choosing an antisocial outcome, and 0 indicates indifference.

Looking frequency was computed based on the average number of gaze shifts landing on the face of the recipient monkey (the face region of the recipient was empirically mapped and fitted with a rectangle window) or the bottle (mapped empirically with the same-dimensioned window as the face region) during the 2.5 sec inter-trial interval[6,27,28,52]. Decision reaction time, the time from the onset of two targets on free-choice trials to eye movement onset, were computed using a 20° sec^{-1} velocity criterion[6,27,28,52].

Spiking and LFP activity

Broadband analog signals were amplified, band-pass filtered (250 Hz–8 kHz), and digitized (40 kHz) using a Plexon OmniPlex system. Spiking data were saved for waveform verifications offline and automatically sorted using the MountainSort algorithm[53]. LFP data were analyzed using custom MATLAB scripts (The MathWorks) and the Chronux signal processing toolbox[54]. Continuous LFP signals from each recording electrode in each area were segmented into 1 sec periods centered on

552 acquiring the choice target or acquiring the central cue at a sample rate of 1 kHz. Raw signals were then
553 band-passed filtered from 2.5 Hz to 250 Hz. We chose a zero-phase filter to avoid introducing phase-
554 distortions to the signals. Signals were normalized by subtracting a reference voltage trace recorded from
555 an independent reference electrode placed in the subdural space in order to eliminate the common noise
556 from each electrode. Three primary epochs were used to carry out neural data analyses: during the 150 ms
557 window during the first fixation period required to begin each trial (baseline epoch); during the 100 ms
558 period centered on the time of acquiring a choice target on free-choice trials (decision epoch); and during
559 the 50–150 ms period after the central cue onset on forced-choice trials (cue epoch).
560

561 **Spike-field coherence and field-field coherence**

562 We quantified spike-field coherence level by examining the phase differences between LFP and
563 spike signals. We designated one area as the "spike contributor" and the other area as the "field
564 contributor". Spike-field coherence was calculated from two directions, either ACCg or BLA as the spike
565 contributor and the other area in the pair as the field contributor. We first binned spikes and LFP using
566 sliding time windows of 150 ms, in steps of 50 ms, for a 1 sec interval centered on the time of decision on
567 free-choice trials or the cue onset on forced-choice trials. Fourier estimates were then computed by means
568 of a multi-taper transformation applied to single trial data; we selected a time half-bandwidth product of
569 2, and multiplied the raw signals by 3 Slepian (orthogonal) tapers[55]. With a 1 kHz sampling rate, this
570 yielded a frequency resolution of ~3.096 Hz. Spectral density estimates were additionally restricted to the
571 10–100 Hz interval. The spectrum density of point process (spikes) was transformed by applying fast
572 Fourier transform on the discrete data. Coherence was then calculated between two spectrum densities of
573 continuous process (LFP) and point process (spikes) by computing the cross-spectral density of the two
574 processes (x and y; P_{xy}) with respect to frequency (f), which was normalized by the product of the power
575 spectral densities of each process (P_{xx} and P_{yy}) as a function of frequency (Eq. 2).

576 $$Coherence = \frac{|P_{xy}(f)|^2}{P_{xx}(f)P_{yy}(f)} \quad \text{(Eq. 2)}$$

577 Raw coherence values therefore ranged from 0 to 1, where a perfectly constant phase relationship
578 between the two regions would be indicated by a coherence value of 1 while an absence of any phase
579 relationship would be indicted by a value of 0. We contrasted coherence values between different
580 conditions and obtained average across pairs of cells and LFP sites. For calculating within-region spike-
581 field coherence, we used the same approach described above for between-region spike-field coherence but
582 excluded relating spikes and LFPs originating from the same electrode channels. For looking at the
583 relationships of LFPs across the two regions, field-field coherence was computed in the same format as in
584 the spike-field coherence described above except the following. Field-field coherence was calculated

between two spectrum densities of continuous processes (LFPs from each region) by computing the cross-spectral density of the two processes (*x* and *y;* P_{xy}) with respect to frequency (*f*), which was normalized by the product of the power spectral densities of LFP processes from each region (P_{xx} and P_{yy}) with respect to frequency (same format as in Eq. 2).

Directionality of information flow

We calculated partial directed coherence (PDC), which is based on multivariate autoregressive (MVAR) model and is well suited for describing directionality of information flow between simultaneously recorded time series in the frequency domain[30]. We contrasted time-varying PDC as (*Other*) – (*Bottle*) and (*Self*) – (*Both*) for free-choice trials, as well as (*Other-forced*) – (*Bottle-forced*) and (*Self-forced*) – (*Both-forced*) for forced-choice trials. As we did for the coherence analyses, we restricted the combinations of pairs to be unique across sites. For example, for the data recorded from a 16-channel array placed in each of the two areas, we randomly selected 16 unique pairs out of 16 x 16 pairs to avoid redundancy and undesired inflation in correlations. For each pairwise LFP signals, the parameters of time-varying autoregressive model of order *r* was formulated as:

$$A_r(n) = \begin{bmatrix} a_{ii}^r(n) & a_{ij}^r(n) \\ a_{ji}^r(n) & a_{jj}^r(n) \end{bmatrix} \quad \text{(Eq. 3)}$$

where parameter a reflects time-varying linear relationship between channel i and j at delay r. While $n = 1 \ldots T$ (in 1 ms bins) represents the time dimension, $r = 1 \ldots p$ represents the order of the model. We chose $p = 5$, specifying that the current value is predicted by immediately preceding five values in the series. The model extended to the frequency dimension was defined as:

$$A(n,f) = I - \sum_{r=1}^{p} A_r(n) Z^{-r} \,|_{z=e^{j2\pi f}} \quad \text{(Eq. 4)}$$

where I is the identity matrix and f ranges within 0 to Nyquist frequency. Here, each $A_r(n)$ was estimated with dual extended Kalman filter method[56]. Classical time varying PDC was then defined by taking the absolute value of *A(n,f)* and normalizing by its column vector. To reduce the co-variability of power between channels, we adapted the extended version of classical PDC[57]. The new orthogonalized measure of PDC (ψ) as a function of time and frequency was defined as:

$$\psi_{ij}(n,f) \frac{|Real\{A_{ij}(n,f)\}|}{\sqrt{a_j^H(n,f) a_j(n,f)}} \cdot \frac{|Imag\{A_{ij}(n,f)\}|}{\sqrt{a_j^H(n,f) a_j(n,f)}}, \;\; i \neq j \quad \text{(Eq. 5)}$$

where a_j is the j's column vector and A_{ij} is the ijth element of $A(n,f)$. H denotes the Hamilton transpose of the vector a. For one pair of channels, ψ was shown in a 2 x 2 matrix, where non-diagonal elements represent directional interaction between channel i and j, that is, ACCg→BLA or BLA→ACCg. We then calculated and averaged ψ across all trials in each condition (*Self*, *Both*, *Other*, or *Bottle*) and averaged pairwise sites of PDC across all recording sessions. For testing whether specific frequency bands exhibit

617 significantly different PDC values between conditions for each ACCg→BLA and BLA→ACCg, we
618 compared PDC values from a 50 ms window centered on the time of free-choice decision for free-choice
619 trials and a matching time window beginning at 50 ms following cue onset on forced-trials.
620
621 **Linear Discriminant analysis (LDA)**
622 To test the decodability of social decisions directly from spike-field coherence values, we used a
623 standard linear classifier for population decoding[58]. The analysis was run separately for each time-
624 frequency bin (150 ms bin with 50 ms steps) and for each decision context. For a given time-frequency
625 bin and context, the trial-level vector of spike-field coherence values in that bin was extracted, along with
626 the corresponding vector of decision outcomes for each trial. This outcome vector contained *Other* and
627 *Bottle* labels or *Self* and *Both* labels, depending on the decision context. The decoder was therefore trained
628 to discriminate between binary outcomes on the basis of spike-field coherence values. In the training
629 phase, 75% of trials were selected at random to train the classifier model. In the testing phase, coherence
630 values for the remaining 25% of trials were used as inputs, yielding estimates of the decision outcome on
631 each trial.
632 Decoder performance was assessed as the percentage of test-phase trials that were correctly
633 labeled. The statistical significance of the performance was assessed with a permutation test. For each of
634 100 iterations, a null value of the decoder's performance was obtained by shuffling the decision outcome
635 labels before training and testing. The analysis thus produced arrays of matching sizes representing the
636 real and null decoding performance for each (time, frequency, condition, iteration) sequence. Decoding
637 was considered significant if the average performance was higher than the corresponding null
638 performance at least 99% of the time ($p < 0.01$, FDR-corrected for multiple comparisons across
639 frequencies).
640
641

References

1. Behrens, T. E. J., Hunt, L. T. & Rushworth, M. F. S. The computation of social behavior. *Science* **324**, 1160–1164 (2009).
2. Bhanji, J. P. & Delgado, M. R. The social brain and reward: social information processing in the human striatum. *Wiley Interdiscip. Rev. Cogn. Sci.* **5**, 61–73 (2014).
3. Sliwa, J. & Freiwald, W. A. A dedicated network for social interaction processing in the primate brain. *Science* **356**, 745–749 (2017).
4. Ruff, C. C. & Fehr, E. The neurobiology of rewards and values in social decision making. *Nat. Rev. Neurosci.* **15**, 549–562 (2014).
5. Seo, H. & Lee, D. Neural basis of learning and preference during social decision-making. *Curr. Opin. Neurobiol.* **22**, 990–995 (2012).
6. Chang, S. W. C., Gariépy, J.-F. & Platt, M. L. Neuronal reference frames for social decisions in primate frontal cortex. *Nat. Neurosci.* **16**, 243–250 (2013).
7. Haroush, K. & Williams, Z. M. Neuronal prediction of opponent's behavior during cooperative social interchange in primates. *Cell* **160**, 1233–1245 (2015).
8. Noritake, A., Ninomiya, T. & Isoda, M. Social reward monitoring and valuation in the macaque brain. *Nat. Neurosci.* **21**, 1452–1462 (2018).
9. Chang, S. W. C. *et al.* Neural mechanisms of social decision-making in the primate amygdala. *Proc. Natl. Acad. Sci.* **112**, 16012–16017 (2015).
10. Grabenhorst, F., Báez-Mendoza, R., Genest, W., Deco, G. & Schultz, W. Primate Amygdala neurons simulate decision processes of social partners. *Cell* **177**, 986-998.e15 (2019).
11. Munuera, J., Rigotti, M. & Salzman, C. D. Shared neural coding for social hierarchy and reward value in primate amygdala. *Nat. Neurosci.* **21**, 415–423 (2018).
12. Azzi, J. C. B., Sirigu, A. & Duhamel, J.-R. Modulation of value representation by social context in the primate orbitofrontal cortex. *Proc. Natl. Acad. Sci.* **109**, 2126–2131 (2012).
13. Baez-Mendoza, R., Harris, C. J. & Schultz, W. Activity of striatal neurons reflects social action and own reward. *Proc. Natl. Acad. Sci.* **110**, 16634–16639 (2013).
14. Falcone, R., Brunamonti, E., Ferraina, S. & Genovesio, A. Neural encoding of self and another agent's goal in the primate prefrontal cortex: human-monkey interactions. *Cereb. Cortex* **26**, 4613–4622 (2016).
15. Nummela, S. U., Jovanovic, V., Mothe, L. de la & Miller, C. T. Social Context-dependent activity in marmoset frontal cortex populations during natural conversations. *J. Neurosci.* **37**, 7036–7047 (2017).

16. Apps, M. A. J., Rushworth, M. F. S. & Chang, S. W. C. The anterior cingulate gyrus and social cognition: tracking the motivation of others. *Neuron* **90**, 692–707 (2016).
17. Hill, M. R., Boorman, E. D. & Fried, I. Observational learning computations in neurons of the human anterior cingulate cortex. *Nat. Commun.* **7**, 12722 (2016).
18. Zaki, J. & Ochsner, K. The neuroscience of empathy: progress, pitfalls and promise. *Nat. Neurosci.* **15**, 675–680 (2012).
19. Mars, R. B. *et al.* On the relationship between the "default mode network" and the "social brain". *Front. Hum. Neurosci.* **6**, (2012).
20. Amadei, E. A. *et al.* Dynamic corticostriatal activity biases social bonding in monogamous female prairie voles. *Nature* **546**, 297–301 (2017).
21. Allsop, S. A. *et al.* Corticoamygdala transfer of socially derived information gates observational learning. *Cell* **173**, 1329-1342.e18 (2018).
22. Zhan, Y. *et al.* Deficient neuron-microglia signaling results in impaired functional brain connectivity and social behavior. *Nat. Neurosci.* **17**, 400–406 (2014).
23. Carmichael, S. T. & Price, J. L. Limbic connections of the orbital and medial prefrontal cortex in macaque monkeys. *J. Comp. Neurol.* **363**, 615–641 (1995).
24. Klavir, O., Genud-Gabai, R. & Paz, R. Functional connectivity between amygdala and cingulate cortex for adaptive aversive learning. *Neuron* **80**, 1290–1300 (2013).
25. Pesaran, B. *et al.* Investigating large-scale brain dynamics using field potential recordings: analysis and interpretation. *Nat. Neurosci.* **21**, 903 (2018).
26. Fries, P. A mechanism for cognitive dynamics: neuronal communication through neuronal coherence. *Trends Cogn. Sci.* **9**, 474–480 (2005).
27. Chang, S. W. C., Winecoff, A. A. & Platt, M. L. Vicarious reinforcement in rhesus macaques (*Macaca mulatta*). *Front. Neurosci.* **5**, (2011).
28. Chang, S. W. C., Barter, J. W., Ebitz, R. B., Watson, K. K. & Platt, M. L. Inhaled oxytocin amplifies both vicarious reinforcement and self reinforcement in rhesus macaques (*Macaca mulatta*). *Proc. Natl. Acad. Sci.* **109**, 959–964 (2012).
29. Paxinos, G., Huang, X.-F. & Toga, A. W. *The Rhesus Monkey Brain in Stereotaxic Coordinates*. (Academic Press, 1999).
30. Baccalá, L. A. & Sameshima, K. Partial directed coherence: a new concept in neural structure determination. *Biol. Cybern.* **84**, 463–474 (2001).
31. Buzsáki, G. & Wang, X.-J. Mechanisms of gamma oscillations. *Annu. Rev. Neurosci.* **35**, 203–225 (2012).
32. Fries, P. Rhythms for cognition: Communication through coherence. *Neuron* **88**, 220–235 (2015).

33. Pesaran, B. *et al.* Investigating large-scale brain dynamics using field potential recordings: analysis and interpretation. *Nat. Neurosci.* **21**, 903–919 (2018).
34. Hipp, J. F., Engel, A. K. & Siegel, M. Oscillatory synchronization in large-scale cortical networks predicts perception. *Neuron* **69**, 387–396 (2011).
35. Womelsdorf, T., Fries, P., Mitra, P. P. & Desimone, R. Gamma-band synchronization in visual cortex predicts speed of change detection. *Nature* **439**, 733–736 (2006).
36. Wong, Y. T., Fabiszak, M. M., Novikov, Y., Daw, N. D. & Pesaran, B. Coherent neuronal ensembles are rapidly recruited when making a look-reach decision. *Nat. Neurosci.* **19**, 327–334 (2016).
37. Kahana, M. J., Sekuler, R., Caplan, J. B., Kirschen, M. & Madsen, J. R. Human theta oscillations exhibit task dependence during virtual maze navigation. *Nature* **399**, 781–784 (1999).
38. Fujisawa, S. & Buzsáki, G. A 4 Hz oscillation adaptively synchronizes prefrontal, VTA, and hippocampal activities. *Neuron* **72**, 153–165 (2011).
39. Adhikari, A., Topiwala, M. A. & Gordon, J. A. Synchronized activity between the ventral hippocampus and the medial prefrontal cortex during anxiety. *Neuron* **65**, 257 (2010).
40. Antzoulatos, E. G. & Miller, E. K. Increases in functional connectivity between prefrontal cortex and striatum during category learning. *Neuron* **83**, 216–225 (2014).
41. Brincat, S. L. & Miller, E. K. Frequency-specific hippocampal-prefrontal interactions during associative learning. *Nat. Neurosci.* **18**, 576–581 (2015).
42. Taub, A. H., Perets, R., Kahana, E. & Paz, R. Oscillations synchronize amygdala-to-prefrontal primate circuits during aversive learning. *Neuron* **97**, 291-298.e3 (2018).
43. Buschman, T. J. & Miller, E. K. Top-down versus bottom-up control of attention in the prefrontal and posterior parietal cortices. *Science* **315**, 1860–1862 (2007).
44. Engel, A. K., Fries, P. & Singer, W. Dynamic predictions: oscillations and synchrony in top-down processing. *Nat. Rev. Neurosci.* **2**, 704–716 (2001).
45. Engel, A. K. & Fries, P. Beta-band oscillations--signalling the status quo? *Curr. Opin. Neurobiol.* **20**, 156–165 (2010).
46. Cardin, J. A. *et al.* Driving fast-spiking cells induces gamma rhythm and controls sensory responses. *Nature* **459**, 663–667 (2009).
47. Jia, X. & Kohn, A. Gamma rhythms in the brain. *PLOS Biol.* **9**, e1001045 (2011).
48. Livneh, U., Resnik, J., Shohat, Y. & Paz, R. Self-monitoring of social facial expressions in the primate amygdala and cingulate cortex. *Proc. Natl. Acad. Sci.* **109**, 18956–18961 (2012).
49. Gothard, K. M., Battaglia, F. P., Erickson, C. A., Spitler, K. M. & Amaral, D. G. Neural responses to facial expression and face identity in the monkey amygdala. *J. Neurophysiol.* **97**, 1671–1683 (2007).

50. Grabenhorst, F., Hernádi, I. & Schultz, W. Prediction of economic choice by primate amygdala neurons. *Proc. Natl. Acad. Sci.* **109**, 18950–18955 (2012).
51. Liu, Y., Yttri, E. A. & Snyder, L. H. Intention and attention: different functional roles for LIPd and LIPv. *Nat. Neurosci.* **13**, 495–500 (2010).
52. Chang, S. W. *et al.* Neural mechanisms of social decision-making in the primate amygdala. *Proc. Natl. Acad. Sci.* **112**, 16012–16017 (2015).
53. Chung, J. E. *et al.* A fully automated approach to spike sorting. *Neuron* **95**, 1381-1394.e6 (2017).
54. Bokil, H., Andrews, P., Kulkarni, J. E., Mehta, S. & Mitra, P. P. Chronux: a platform for analyzing neural signals. *J. Neurosci. Methods* **192**, 146–151 (2010).
55. Jarvis, M. R. & Mitra, P. P. Sampling properties of the spectrum and coherency of sequences of action potentials. *Neural Comput.* **13**, 717–749 (2001).
56. Sommerlade, L. *et al.* Time-variant estimation of directed influences during Parkinsonian tremor. *J. Physiol. Paris* **103**, 348–352 (2009).
57. Omidvarnia, A. H. *et al.* Orthogonalized Partial Directed Coherence for Functional Connectivity Analysis of Newborn EEG. in *Neural Information Processing* (eds. Huang, T., Zeng, Z., Li, C. & Leung, C. S.) 683–691 (Springer Berlin Heidelberg, 2012).
58. Saez, A., Rigotti, M., Ostojic, S., Fusi, S. & Salzman, C. D. Abstract Context Representations in Primate Amygdala and Prefrontal Cortex. *Neuron* **87**, 869–881 (2015).

Supplementary Results

Field-field coherence between ACCg and BLA are qualitatively different from spike-field coherence

The spike-field relations between ACCg and BLA (**Fig. 3**) were qualitatively different from the relations found between LFP themselves across the two regions. The field-field coherence patterns were examined from 447 ACCg sites (241 and 206 sites in monkey H and K, respectively) and 402 BLA sites (211 and 191 sites in monkey H and K). When we analyzed the decision epoch where we observed the enhancements in the spike-field coherence for prosocial decision preference over antisocial decision preference, we found no significant field-field coherence patterns in the gamma band for prosocial compared to antisocial decisions preference ($p = 0.81$, Wilcoxon sign rank) (**Fig. S3**). Rather, we observed significantly suppressed field-field coherence values in the beta band for prosocial compared to antisocial decision preference ($p < 0.01$) (**Fig. S3**). Therefore, the observed spike-field coherence patterns differentiating prosocial from antisocial decision preference (**Fig. 3**) are not likely to be simply driven by common input signals to both ACCg and BLA as these should be reflected in their field-field coherence patterns.

Local spike-field coherence within ACCg and BLA

We also examined local-level relations between spiking and LFP activity within each region. The $ACCg_{spike}$-$ACCg_{field}$ coherence increased around the time of free-choice decision in the gamma band for prosocial relative to antisocial decision preference ($p < 0.0001$, Wilcoxon sign rank; **Fig. S4a**). This coherence difference was absent on forced-choice trials when the computer determined the outcomes ($p = 0.13$, Wilcoxon sign rank; **Fig. S4b**). By contrast, the BLA_{spike}-BLA_{field} coherence increased diffusely around the time of free-choice decision not only in the beta band but also in a much wider gamma range for prosocial relative to antisocial decision preference (both beta and gamma, $p < 0.0001$, Wilcoxon sign rank; **Fig. S4a**), with weaker coherence difference in the absence of decision-making (both beta and gamma, $p < 0.0001$) (**Fig. S4b**).

Supplementary Figures (S1–S5)

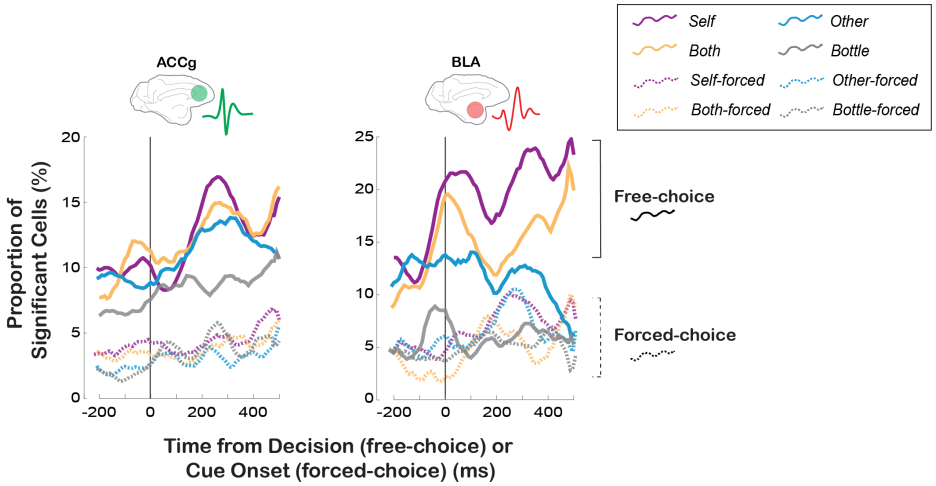

Fig. S1. Single neuron summary for encoding *Self*, *Other*, *Both*, and *Bottle* reward outcomes for free-choice and forced-choice trials in BLA and ACCg. Proportions of all recorded cells in ACCg (left) and BLA (right) that exhibited significant firing rate modulations in *Self* (purple), *Both* (orange), *Other* (blue), or *Bottle* (gray) condition across time relative to the baseline fixation epoch ($p < 0.05$, Wilcoxon sign rank). Data from free-choice trials (solid lines) are aligned to the time of decision, whereas data from forced-choice trials (dashed lines) are aligned to the time of cue onset.

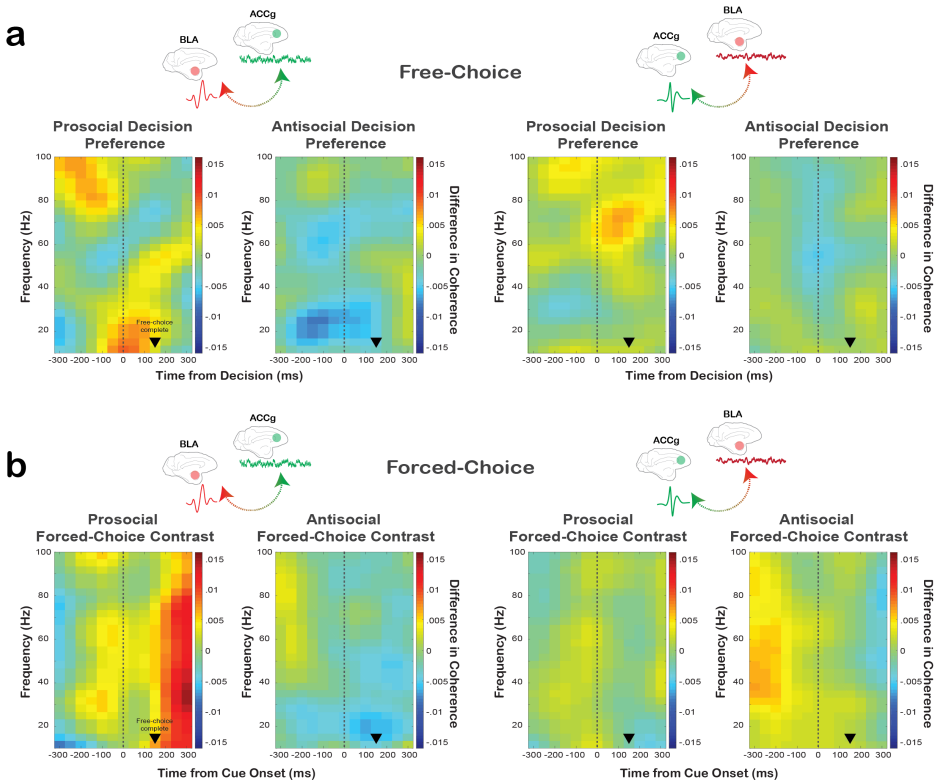

Fig. S2. Spike-field coherence between ACCg and BLA cells separately for prosocial and antisocial decision preference as well as prosocial and antisocial forced-choice contrast. (**a**) BLA_{spike}–$ACCg_{field}$ coherence (left) and $ACCg_{spike}$–BLA_{field} coherence (right) across time and frequency separately for when monkeys actively expressed either prosocial (choosing *Other* over *Bottle*, *Other–Bottle*) or antisocial decision preference (choosing *Self* over *Both*, *Self–Both*) on free-choice trials. Data are aligned to the time of decision on free-choice trials. (**b**) BLA_{spike}–$ACCg_{field}$ coherence (left) and $ACCg_{spike}$–BLA_{field} coherence (right) across time and frequency separately for when monkeys were presented with computer-determined outcomes on forced-choice trials, contrasting *Other-forced* over *Bottle-forced* to generate prosocial forced-choice contrast (*Other-forced – Bottle-forced*) and *Self-forced* over *Both-forced* to generate antisocial forced-choice contrast (*Self-forced – Both-forced*). Thus, these forced-choice contrasts matched the contrasts used for prosocial decision preference (choosing *Other* over *Bottle*) and antisocial decision preference (choosing *Self* over *Both*) with respect to reward outcome. Data are aligned to the time of cue onset on forced-choice trials. In all plots, the black arrowheads mark the time at which the monkeys completed a free-choice or forced-choice decision by maintaining fixation on a chosen target or cue for 150 ms.

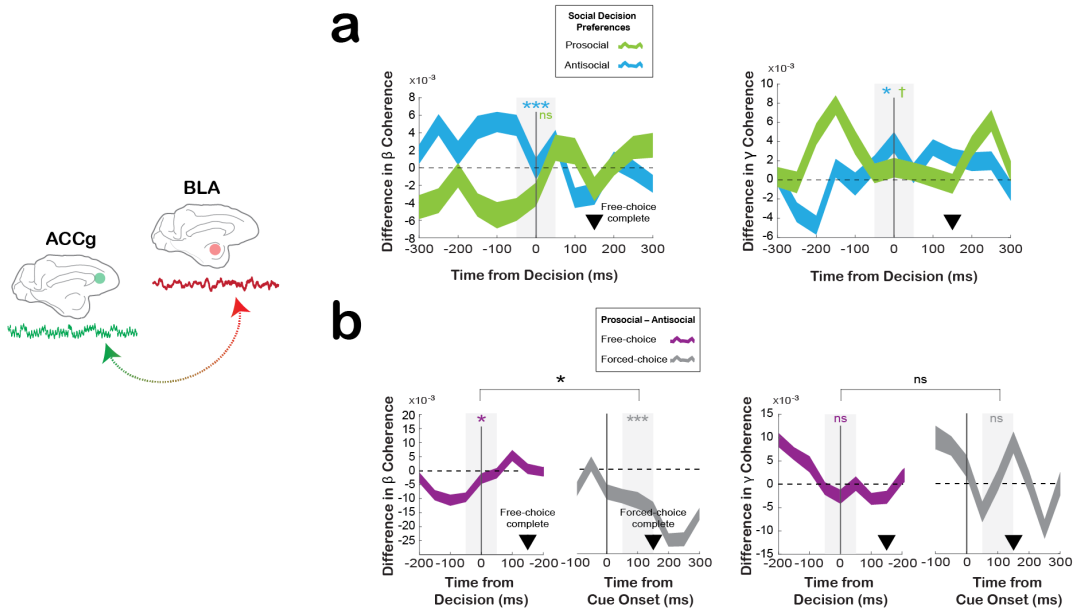

Fig. S3. Field-field coherence between ACCg and BLA shows qualitatively different patterns. (**a**) Time courses of the field-field coherence values in the beta frequency (15–25 Hz; left) and the gamma frequency (45–70 Hz; right) separately for prosocial (light green; *Other–Bottle*) and antisocial (light blue; *Self–Both*) preferences. Significant coherence differences relative to zero are indicated by asterisks of the matching colors for the same time windows used for the spike-field coherence analyses. (**b**) Time courses of the same beta (left) and gamma (right) band field-field coherence contrasting between prosocial and antisocial decision preferences on free-choice trials (purple) and contrasting prosocial and antisocial forced-choice contrasts on forced-choice trials (grey). In both **a** and **b**, significant coherence differences from zero (Wilcoxon sign rank) are indicated by asterisks in the matching colors and significant coherence differences between the traces (Wilcoxon rank sum) are indicated in black asterisks for the analyzed epoch (gray shading) (***, $p < 0.0001$; **, $p < 0.001$; *, $p < 0.01$; †, $p = 0.07$; ns, not significant). In all panels, the black arrowheads mark the time at which the monkeys completed a free-choice or forced-choice decision by maintaining fixation on a chosen target or cue for 150 ms.

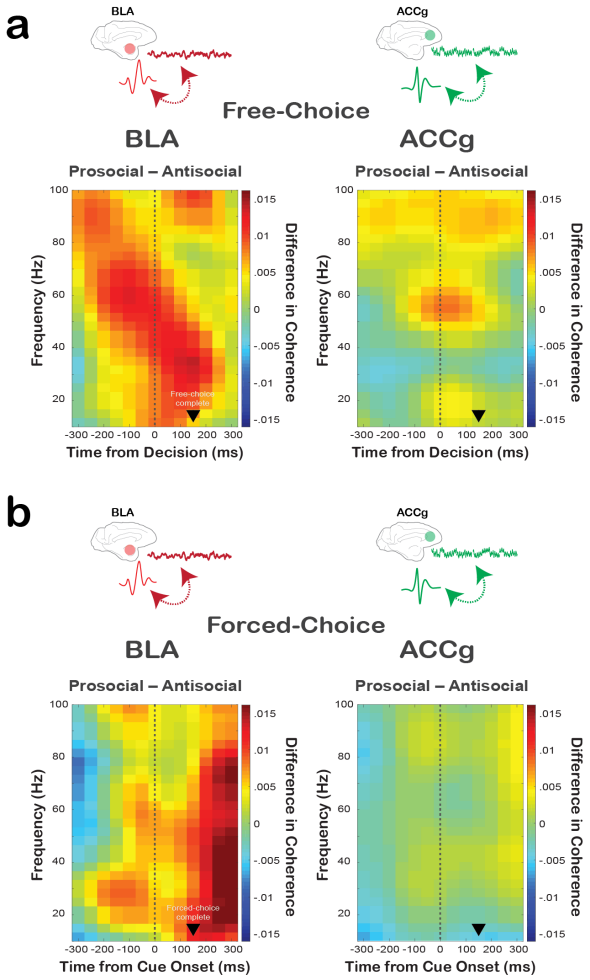

Fig. S4. Local, within-region spike-field coherence in ACCg and BLA for prosocial compared to antisocial decision preference. (**a**) Differences in BLA_{spike}-BLA_{field} coherence (left) and $ACCg_{spike}$-$ACCg_{field}$ coherence (right) across time and frequency when monkeys actively expressed prosocial (choosing *Other* over *Bottle*) versus antisocial decision preference (choosing *Self* over *Both*) on free-choice trials. Data are aligned to the time of free-choice decision. (**b**) Differences in BLA_{spike}-BLA_{field} coherence (left) and $ACCg_{spike}$-$ACCg_{field}$ coherence (right) across time and frequency when monkeys were presented with computer-determined outcomes on forced-choice trials, contrasting *Other-forced* over *Bottle-forced* to generate prosocial forced-choice contrast and *Self-forced* over *Both-forced* to generate antisocial forced-choice contrast (thus, matching the contrasts across free-choice and forced-choice trials with respect to reward outcome). Data are aligned to the time of cue onset on forced-choice trials. In all panels, the black arrowheads mark the time at which the monkeys completed a free-choice or a forced-choice decision by maintaining the fixation on a target or cue for 150 ms.

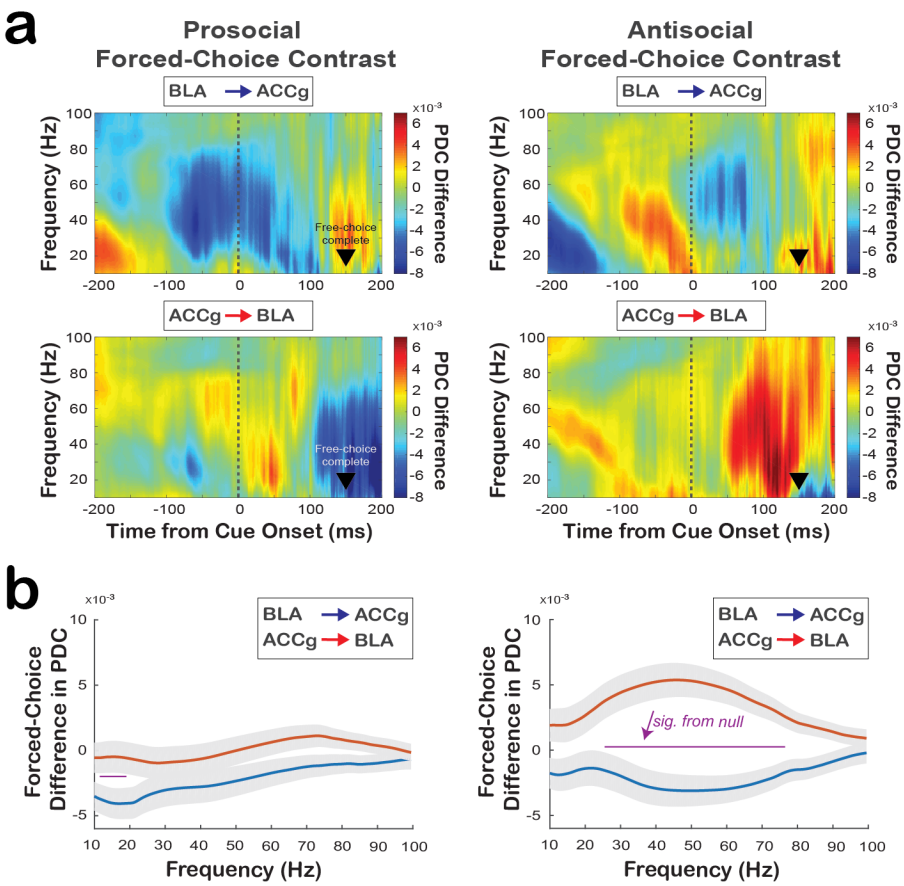

Fig. S5. Directionality of information flow between ACCg and BLA for computer-determined outcomes on forced-choice trials as a function of frequency and time. (a) Frequency-domain directional influences assessed by partial directed coherence (PDC) when monkeys were presented with computer-determined outcomes (forced-choice trials). PDC values as a function of time and frequency for *Other-forced* over *Bottle-forced* (prosocial forced-choice contrast; see the legend in **Fig. S2**) for BLA→ACCg (top left) and ACCg→BLA (bottom left), and PDC values for *Self-forced* over *Both-forced* (antisocial forced-choice contrast) for BLA→ACCg (top right) and ACCg→BLA (bottom right). Data are aligned to the time of cue onset. The black arrowhead marks the time at which the monkeys completed a forced-choice decision. (**b**) Quantifications of the directional information flow on forced-choice trials as a function of frequency for *Other-forced* over *Bottle-forced* (left) and *Self-forced* over *Both-forced* (right). Shown are differences in PDC values for BLA→ACCg (in blue) and ACCg→BLA (in red) during the cue epoch. Horizontal purple lines indicate significant differences between two traces ($p < 0.05$, Wilcoxon sign rank). Shaded regions represent standard errors.